water

MDPI

Article

Enhanced Electricity Generation in Solar-Driven Photo-Bioelectrochemical Cells Equipped with $Co_3(PO_4)_2/Mg(OH)_2$ Photoanode

Razieh Rafieenia [1,*,†], Mohamed Mahmoud [2,3], Mahmoud S. Abdel-Wahed [2], Tarek A. Gad-Allah [2], Anna Salvian [1,4], Daniel Farkas [1], Fatma El-Gohary [2] and Claudio Avignone Rossa [1]

[1] Department of Microbial Sciences, University of Surrey, Guildford GU2 7XH, UK; df00080@surrey.ac.uk (D.F.); c.avignone-rossa@surrey.ac.uk (C.A.R.)
[2] Water Pollution Research Department, National Research Centre, 33 El-Buhouth St., Dokki, Cairo 12311, Egypt; mahmoudsaadnrc@gmail.com (M.S.A.-W.)
[3] Faculty of Engineering, Galala University, Galala City, Suez 43511, Egypt
[4] School of Chemistry and Chemical Engineering, University of Surrey, Guildford GU2 7XH, UK
* Correspondence: r.rafieenia@imperial.ac.uk
† Current address: Department of Bioengineering, Imperial College London, London SW7 2AZ, UK.

Abstract: We developed a solar-driven photo-bioelectrochemical cell (s-PBEC) employing a novel anode photocatalyst material ($Co_3(PO_4)_2/Mg(OH)_2$) intimately coupled with electrochemically active bacteria for synergic electricity generation from wastewater. An s-PBEC was inoculated with a natural microbial community and fed with synthetic wastewater to analyze the performance of the system for electricity generation. Linear sweep voltammetry indicated an increase in power output upon light illumination of the s-PBEC after 1 h, rising from 66.0 to 91.5 mW/m^2. The current density in the illuminated s-PBEC exhibited a rapid increase, reaching 0.32 A/m^2 within 1 h, which was significantly higher than the current density in dark conditions (0.15 A/m^2). Shotgun metagenomic analysis revealed a significant shift in the microbial community composition with a more diverse anodic biofilm upon illumination compared to the microbial communities in dark conditions. Three unclassified genera correlated with the enhanced current generation in illuminated s-PBEC, including *Neisseriales* (16.31%), *Betaproteobacteria* (7.37%), and *Alphaproteobacteria* (5.77%). This study opens avenues for further exploration and optimization of the solar-driven photo-bioelectrochemical cells, paving the way for integrative approaches for sustainable energy generation and wastewater treatment.

Keywords: wastewater treatment; solar-driven photo-bioelectrochemical cells; photocatalysis; $Co_3(PO_4)_2/Mg(OH)_2$; biodegradation; microbial community

check for updates

Citation: Rafieenia, R.; Mahmoud, M.; Abdel-Wahed, M.S.; Gad-Allah, T.A.; Salvian, A.; Farkas, D.; El-Gohary, F.; Avignone Rossa, C. Enhanced Electricity Generation in Solar-Driven Photo-Bioelectrochemical Cells Equipped with $Co_3(PO_4)_2/Mg(OH)_2$ Photoanode. *Water* **2024**, *16*, 1683. https://doi.org/10.3390/w16121683

Academic Editor: Hassimi Abu Hasan

Received: 24 April 2024
Revised: 11 June 2024
Accepted: 12 June 2024
Published: 13 June 2024

Copyright: © 2024 by the authors. Licensee MDPI, Basel, Switzerland. This article is an open access article distributed under the terms and conditions of the Creative Commons Attribution (CC BY) license (https://creativecommons.org/licenses/by/4.0/).

1. Introduction

Human-induced activities that arise from industrialization consistently introduce a diverse range of pollutants into terrestrial and aquatic environments. Certain recalcitrant organic pollutants emerge as contaminants of high concern due to continuous discharges from industries, hospital effluents, and households into the environment. Despite their low concentrations in municipal wastewater and surface water (ranging from ng/L to µg/L), these pollutants remain biologically active, posing adverse effects on humans, animals, and aquatic organisms. Some examples include pharmaceuticals, personal care products, and pesticides [1]. In many countries, these compounds are released into municipal wastewater systems without pre-treatment and subsequently directed to wastewater treatment plants. Conventional wastewater treatment technologies (primary treatment followed by activated sludge) can only partially remove them [2]. The presence of these contaminants in surface and groundwaters, as well as sewage systems, poses a pervasive problem with associated risks to ecosystems and human health, including acute ecotoxicity and endocrine

disruption [3,4]. The need for environmentally friendly technologies that can address the challenges posed by persistent organic contaminants has become increasingly apparent.

Microbial electrochemical systems (MESs) are considered an emerging technology that integrates biodegradation and electrochemical processes to simultaneously treat wastewater and generate renewable energy [5–8]. Owing to the synergy between electrochemical processes and electrochemically active bacteria (EAB), MESs have attracted significant interest as a sustainable approach to efficiently convert chemical energy stored in wastewater into a wide spectrum of value-added products and renewable energy [9,10]. More importantly, this integration holds promise for overcoming some limitations inherent in traditional biodegradation and electrochemical systems, resulting in enhanced treatment efficiencies compared to standalone processes [1,11]. The hallmark of MESs is the ability of EAB to oxidize organic compounds and facilitate the extracellular transfer of the resulting electrons into the anode surface. Nevertheless, one of the challenges facing scaling up MESs is the low energy output and substrate utilization rate. Thus, the choice of anode materials is crucial for enhancing extracellular electron transfer (EET) and the overall performance of MESs since they serve as a harbour for EAB, therefore affecting biofilm colonization and the electron transfer resistance into the anode surface [12,13].

Among several options, the integration of bioanodes and abiotic photoanodes opens new opportunities for converting recalcitrant contaminants to electricity and expediting the EET rate in MESs [14]. For instance, intimate coupling photocatalysis and biodegradation (ICPB) represents a promising approach to reducing the toxicity of recalcitrant compounds on microorganisms and increasing their biodegradation [15]. The ICPB concept has been studied in various reactor configurations, and recently, it has been reported as a novel approach to be applied in MESs to improve the degradability of recalcitrant pollutants and reduce their toxicity on EAB [1]. To date, the development of MESs with ICPB photoelectrodes has been reported by a limited number of studies [16–19]. The ICPB photoelectrodes are usually made of a macroporous carrier, such as carbon foam, coated with a photocatalyst. Photocatalysis relies on the electron transfer from the valence band (VB) to the conduction band (CB) of the photocatalyst upon light illumination, resulting in the generation of highly reactive oxygen species (ROSs) and transforming the recalcitrant compounds to more readily biodegradable compounds that can be efficiently consumed by EAB [17,18,20,21]. Thus, the synergy between photocatalytic oxidation and microbial degradation could result in enhanced pollutant removal and high-power output [22]. More importantly, the three-dimensional porous architecture of the ICPB photoanode protects EAB from damage by ROSs. In this unique configuration, electroactive biofilms are allowed to grow inside the pores of the electrodes, positioning them away from the area where ROSs are produced on the photoanode's surface, but yet near enough for the bacteria to efficiently consume photocatalytic readily biodegradable by-products [1].

In this context, two-dimensional (2D) materials have shown higher efficiency in photocatalytic applications owing to their superior features, such as high specific surface area, high photon-harvesting efficiency, and low exciton recombination rate [23,24]. Recently, 2D cobalt phosphate ($Co_3(PO_4)_2$) has attracted the attention of photocatalysis research owing to its low cost, narrow band gap (2.32 eV), strong capability to harvest visible light, and environmental compatibility [25]. However, its narrow band gap might facilitate the recombination between the charge carriers, which, in turn, limits its photocatalytic efficiency. On the other hand, magnesium hydroxide ($Mg(OH)_2$) monolayers showed prospective photocatalytic activity for the photodegradation of organic dyes (e.g., methyl orange, rhodamine B, and malachite green). However, its wide direct band gap of 4.74 eV represents a bottleneck for its use in the visible-light region [26]. Thus, $Co_3(PO_4)_2$ seems to have suitable band positions for photocatalytic activity, which is compatible with the energy levels of $Mg(OH)_2$, making this mixed heterojunction photocatalyst effective material to overcome charge recombination issues and enhance photocatalytic activity.

In this study, we developed a 2D/2D $Co_3(PO_4)_2/Mg(OH)_2$ heterojunction photoanode to improve power output in solar-driven photo-bioelectrochemical cells (s-PBEC). First, we

prepared a $Co_3(PO_4)_2/Mg(OH)_2$ heterojunction photocatalyst using a simple precipitation technique. The photocatalyst was deposited on a 3D carbon felt anode, which can be subsequently colonized by EAB. Second, we employed chemical and electrochemical techniques to monitor the improvement in electricity generation and EET in s-PBEC employing $Co_3(PO_4)_2/Mg(OH)_2$ heterojunction photoanode under irradiation. Finally, we analysed the structure and composition of the electroactive biofilm in dark and light conditions using amplicon sequencing.

2. Materials and Methods

2.1. Chemicals

All chemicals used in this study, including cobalt nitrate hexahydrate ($Co(NO_3)_2{\cdot}6H_2O$), diammonium hydrogen phosphate ($(NH_4)_2HPO_4$), magnesium acetate tetrahydrate ($(CH_3COO)_2Mg{\cdot}4H_2O$), ammonia solution ($NH_4OH$, 35%), potassium hexacyanoferrate (III), and those required for media preparation, were purchased from Sigma-Aldrich Co. (UK). They were used as received without further purification.

2.2. Photocatalyst Synthesis and Characterization

Pure and mixed cobalt phosphate ($Co_3(PO_4)_2$) and magnesium hydroxide ($Mg(OH)_2$) photoactive materials have been prepared using a simple precipitation method. For the preparation of pure $Co_3(PO_4)_2$ photocatalyst, 2.38 g of $Co(NO_3)_2{\cdot}6H_2O$ was dissolved in 50 mL of double distilled water. A solution containing 0.72 g of $(NH_4)_2HPO_4$ in 50 mL of double distilled water was dropped slowly on the above cobalt nitrate solution under vigorous stirring. The formed precipitate of $Co_3(PO_4)_2$ was collected by filtration, washed thoroughly with double distilled water, and finally dried at 80 °C for 12 h. Pure $Mg(OH)_2$ was prepared by dissolving 3.68 g $(CH_3COO)_2Mg{\cdot}4H_2O$ in 10 mL of NH_4OH solution. The formed precipitate was treated in a manner similar to the pure $Co_3(PO_4)_2$. In the case of mixed $Co_3(PO_4)_2/Mg(OH)_2$, the pure $Mg(OH)_2$ was dispersed in the aqueous solution of $Co(NO_3)_2{\cdot}6H_2O$ by agitation in an ultrasonic bath for 10 min. Following this, the $(NH_4)_2HPO_4$ solution was slowly added dropwise to allow precipitation of $Co_3(PO_4)_2$ on the surface of $Mg(OH)_2$. Following this procedure, $Co_3(PO_4)_2/Mg(OH)_2$ of 1:1 weight ratio was obtained.

X-ray diffraction (XRD) patterns were collected using a PANalytical X'Pert Pro diffractometer (The Netherlands) with Cu Kα radiation (λ = 0.15406 nm, 40 kV, 15 mA). The traces were recorded within 2θ ranging from 10° to 60° with a scan rate of 10° min^{-1} and a step size of 0.2°. Raman spectra were measured on a confocal Raman microscope (WITec alpha 300 RA) equipped with 785 nm excitation wavelength and 25 mW laser power. Morphology was examined under a high-resolution transmission electron microscope (HR-TEM) (JEOL TEM-2100, Japan). UV–Vis diffuse reflectance spectra (DRS) were recorded within the range 200–1000 nm by a JASCO spectrophotometer (Model V730, Japan) equipped with diffuse reflectance accessories, using $BaSO_4$ as the reference material. The photoluminescence emission spectra were measured using a JASCO FP-6500 fluorescence spectrophotometer equipped with a xenon flash lamp excitation source.

2.3. Enrichment and Acclimatization of EAB

The initial inoculum used in the present study was anaerobic digestion sludge collected from Goddards Green Wastewater Treatment Works (Hassocks, UK). The anode and cathode compartments were separated using a cation exchange membrane (CMI-7000, Membranes Int., USA). The electrode material used for the anode and cathode was carbon felt (Alfa Aesar, ThermoFisher, UK) with dimensions of 25 mm × 25 mm. The anode compartment was filled with a medium with the following components (per L of deionized water): CH_3COONa, 1 g; Na_2HPO_4, 6.02 g; KH_2PO_4, 1.02 g; NH_4Cl, 0.41 g; and trace mineral solution, 10 mL [27]. For acclimating EAB, initially, an external resistance of 1000 Ω was used. The catholyte solution was prepared by dissolution of 4 g potassium hexacyanoferrate (III) in (1:9 v/v) PBS buffer. The catholyte solution was renewed once every 7 days

to avoid the impact of proton accumulation on the current generation. Nitrogen gas was purged into the anolyte for 3 min to ensure an anaerobic environment. The anodic biofilm was collected to be used as inoculum in the s-PBEC. The cells were resuspended in the anolyte solution before inoculation.

2.4. Integration of Photocatalysis and Biodegradation in s-PBEC

Double-chamber reactors equipped with a quartz window for an anodic compartment (Redoxme AB, Sweden) were used. The anode electrode was carbon foam coated with photocatalyst $Co_3(PO_4)_2/Mg(OH)_2$, and carbon felt was used as the cathode material. The composition of the medium used for the s-PBEC was similar to the medium used for microbial enrichment. The s-PBEC bioreactors were operated with an external resistance of 1000 Ω connected between the anode and cathode. All experiments were performed at room temperature (25 ± 2 °C). A solar simulator (Model 10500, ABET Technologies, USA) equipped with a 150 W xenon arc lamp was used to illuminate the reactors. A schematic of the s-PBEC is presented in Figure 1.

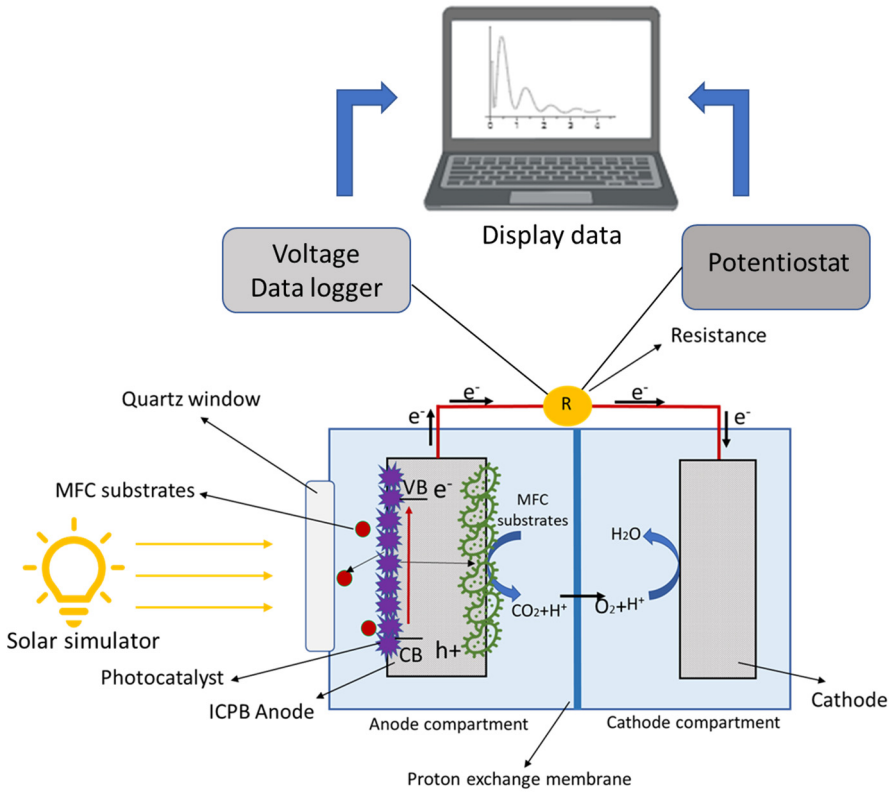

Figure 1. Schematic illustration of the s-PBEC assembly and its working principle.

2.5. Electrochemical Analyses

A data acquisition module (Pico Technology, Cambridge, UK) connected to a personal computer was used to record the voltages (V) generated by the s-PBEC every 2 min. Current generation was calculated from Ohm's law I = V/R, where R is the external resistance. Current densities were calculated by dividing the current generated by s-PBEC by the anode surface area [2.5 cm × 2.5 cm]. The power output (P) of the s-PBECs was calculated according to P = V × I. To analyze the electrochemical activity of anodic biofilm, linear sweep voltammetry (LSV) and electrochemical impedance spectroscopy (EIS) were conducted using a PalmSens potentiostat (PalmSens PS4). The LSV analysis was carried out with a scan rate of 5 mV/s, ranging from open-circuit voltages of MFCs to −0.005 V. The s-PBECs were kept under open circuit conditions for 2 h before the LSV analysis.

EIS measurements were performed within the frequency range of 0.1 to 10 MHz with an amplitude of 10 mV.

2.6. Microbial Community Analysis

At the end of our experiments, total genomic DNA was extracted from the anodic biofilm and initial inoculum using DNeasy PowerSoil Pro Kit (Qiagen, Hilden, Germany) according to the manufacturer's instructions. The quantity and quality of the extracted genomic DNA were quantified by measuring absorbance using a NanoDrop spectrophotometer (Thermo Fisher Scientific) at 260 and 280 nm. High-throughput sequencing was carried out on the Illumina NovaSeq 6000 platform (Illumina Inc., USA) by a commercial party (Novogene, Cambridge, UK) using the bar-coded primer set 515F/806R following the manufacturer's guidelines. The reads were trimmed and quality filtered using Trimmomatic and were assembled using the SqueezeMeta pipeline [28] running in co-assembly mode, with Megahit [29] as the assembler and Maxbin [30] and Metabat [31] as the automatic binners.

3. Results and Discussion

3.1. Physicochemical Characterization of Photocatalyst

We identified the crystal structures of the prepared materials using XRD patterns, as shown in Figure 2a. Despite the low crystallinity of pure cobalt phosphate, the diffraction peak at 2θ of 13.27° that is distinctive for $Co_3(PO_4)_2{\cdot}8H_2O$ phase (ICDD 41-0375) could be observed along with some small confirmatory peaks at 2θ of 18.31°, 23.21°, 27.99°, 30.31°, and 33.22°. The broadness and low intensity of the diffraction peaks indicate the small crystal size of $Co_3(PO_4)_2$. Similarly, (001), (002), and (004) diffraction planes characteristic for $Mg(OH)_2$ (ICDD 01-075-1527) could be identified in the XRD pattern of pure magnesium hydroxide sample. In the samples composed of $Co_3(PO_4)_2$ and $Mg(OH)_2$ mixture, only XRD peaks characteristic for $Mg(OH)_2$ emerged, which might be due to the low peak intensity of $Co_3(PO4)_2$ as mentioned earlier. However, the presence of $Co_3(PO_4)_2$ in those samples was confirmed in the TEM images and Raman spectra, as will be shown later.

For further identification of the formed phases, Raman spectra of pure $Co_3(PO_4)_2$ and $Mg(OH)_2$ and their equiweight mixture were collected and presented in Figure 2b. The bands at 569, 906, 960, and 1059 cm^{-1} can be assigned to the ν4 mode of phosphate ions, P–O–P stretching vibration, P–O stretching vibration, and P–O anti-stretching vibration modes as reported earlier [32,33]. These modes reveal the formation of $Co_3(PO_4)_2$ crystals. Similarly, the bands at 276, 444, and 939 cm^{-1} illustrate the formation of brucite ($Mg(OH)_2$) crystals because these bands originate from E_g mode and a combination of (degenerate) of $A1_g$ and E_gOH modes [34–36]. The recognition of bands that are related to both $Co_3(PO_4)_2$ and $Mg(OH)_2$ further confirms the contact between $Co_3(PO_4)_2$ and $Mg(OH)_2$.

The morphology of the prepared materials was examined using HR-TEM, and the collected images are depicted in Figure 3. Pure $Co_3(PO_4)_2$ samples present 2D thick sheets, as shown in Figure 3a. Each thick sheet is a bundle of very thin sheets comprising tiny spherical particles. The presence of these tiny particles explains the absence of sharp diffraction peaks in the XRD pattern of pure $Co_3(PO_4)_2$. The inset selected area electron diffraction (SAED) in Figure 3a shows a dotted diffraction pattern revealing the high purity of the $Co_3(PO_4)_2$ crystals. In Figure 3b, pure $Mg(OH)_2$ appears as very thin 2D irregular flakes. The circles in the inset SAED discloses the polycrystalline nature of $Mg(OH)_2$. Figure 3c reveals the successful precipitation of $Co_3(PO_4)_2$ on $Mg(OH)_2$. The identification of both components has been conducted based on the individual morphology of each component.

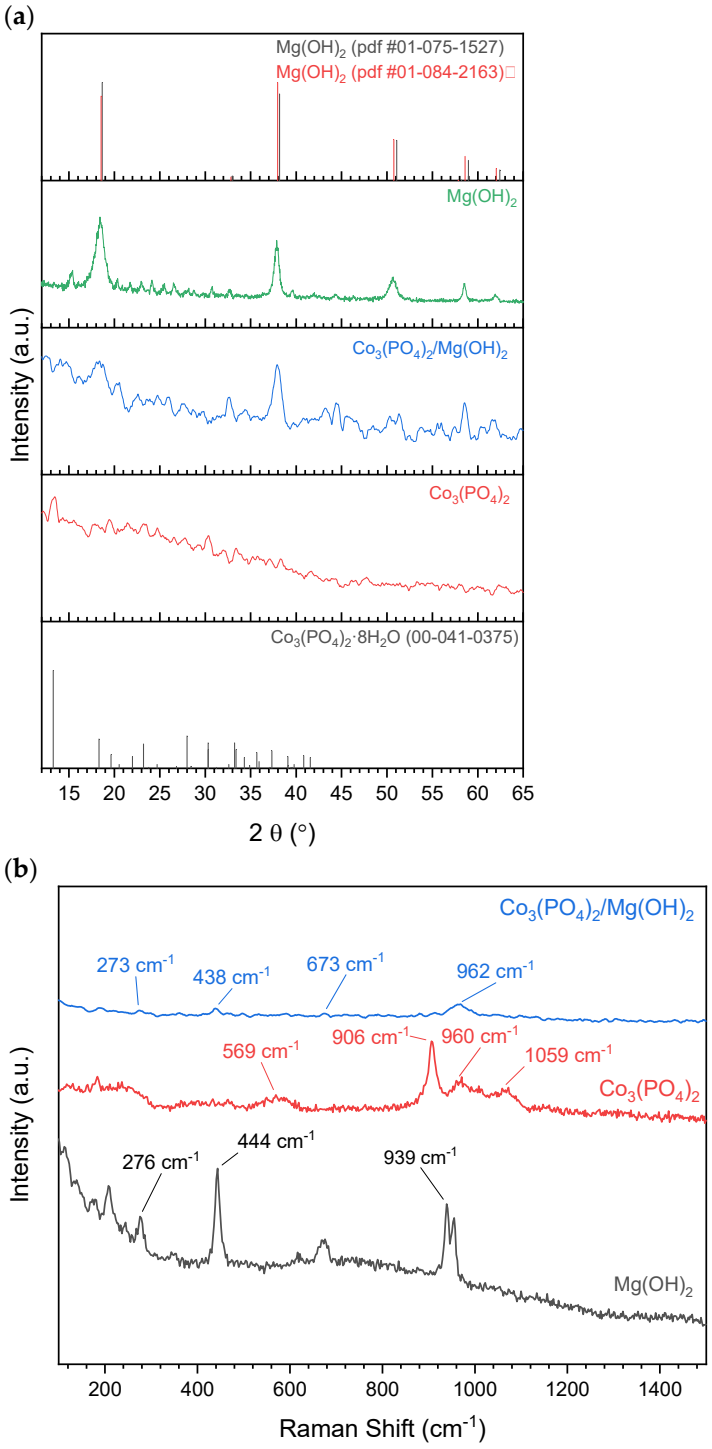

Figure 2. (**a**) XRD patterns and (**b**) Raman spectra of the prepared materials.

Figure 4 shows the optical properties of the pure and composite samples. The spectra in Figure 4a indicate the absorbance of pure $Mg(OH)_2$ only in the UV range, while pure $Co_3(PO_4)_2$ and composite sample exhibit strong absorbance in the visible region too. Hence, it is expected to have good photocatalytic activity under solar irradiation. In order to investigate the charge carrier recombination in the irradiated samples, PL emission spectra upon excitation at 290 nm were detected for all samples (Figure 4b). $Mg(OH)_2$ showed the strongest emission, which is due to its wide band gap. Mixing $Mg(OH)_2$ with the narrower band gap material, $Co_3(PO_4)_2$, caused a reduction in the PL intensity, demonstrating the successful charge transfer within the two materials.

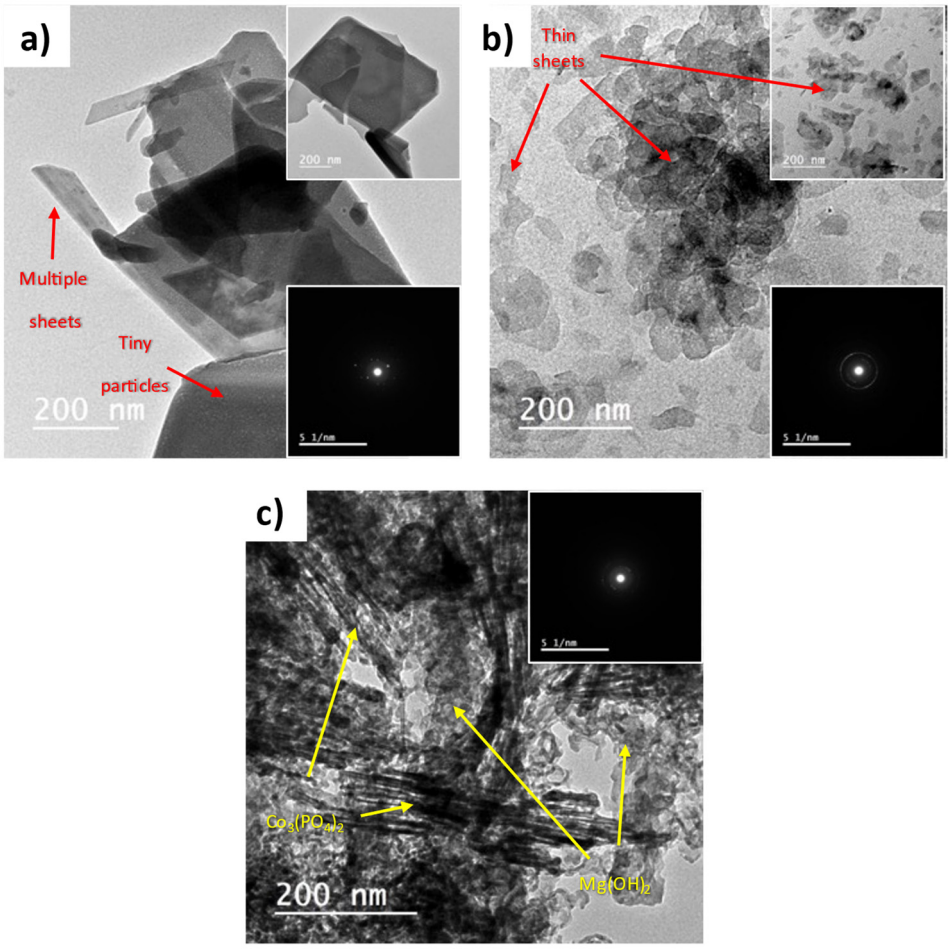

Figure 3. HR-TEM images of (**a**) pure $Co_3(PO4)_2$, (**b**) pure $Mg(OH)_2$, and (**c**) $Co_3(PO_4)_2/Mg(OH)_2$ samples.

3.2. $Co_3(PO_4)_2/Mg(OH)_2$ Heterojunction ICPB Photoanodes Enhance the Performance of s-PBES

Current densities obtained by $Co_3(PO_4)_2/Mg(OH)_2$ heterojunction ICPB photoanodes with and without light exposure (i.e., ICPB (light) and ICPB (dark), respectively) were monitored to investigate the influence of light on the synergistic electricity generation by EAB and subsequent photocatalysts (Figure 5a). A control MFC with an abiotic photoanode (i.e., without inoculation) was employed to assess the current generation solely by the photoanode; the current output of this control MFC was trivial (0.003 A/m^2) (Figure 5b). To investigate the impact of light exposure on electricity generation, the s-PBEC was initially operated in dark mode until a stable current was achieved, which was followed by an illumination phase. The current densities exhibited a rapid increase, starting from 0.15 A/m^2 upon illuminating the ICPB anode, reaching 0.32 A/m^2 within 1 hr, and eventually peaking at 0.38 A/m^2 after almost 2.5 h of light exposure.

Our results are consistent with previous studies, showing an increase in electricity generation after illumination in a single-chamber MFC, wherein a 54% increase in voltage output was achieved using an ICPB anode made of mpg-C_3N_4 photocatalyst [20]. Similarly, another study reported a current density of 0.4 A/m^2 using an ICPB anode made of N-doped TiO_2 photocatalyst, which was almost 50% higher than the current generation by the bioanode (0.28 A/m^2) [17].

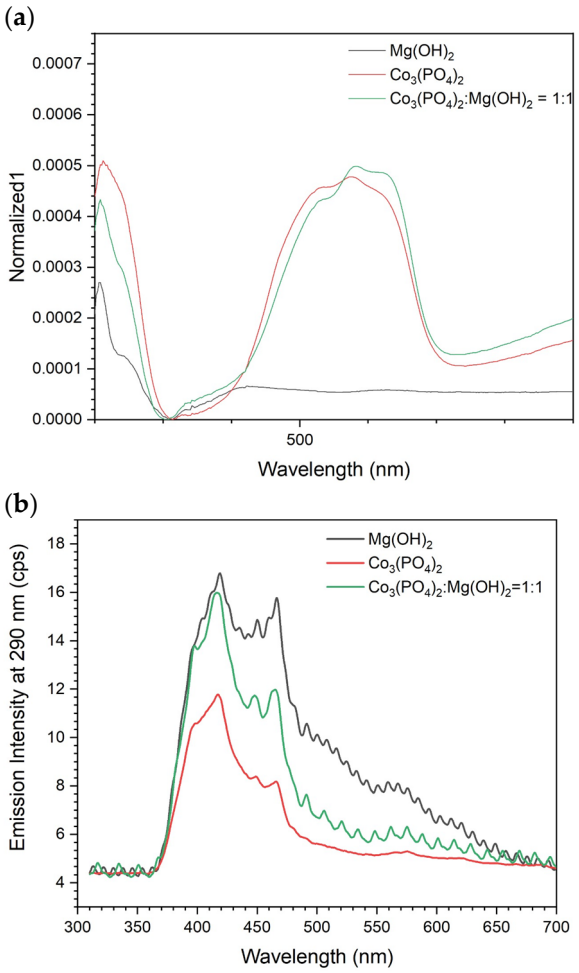

Figure 4. Optical properties of the prepared materials: (**a**) UV–Vis absorbance spectra and (**b**) PL spectra of the prepared electrocatalysts.

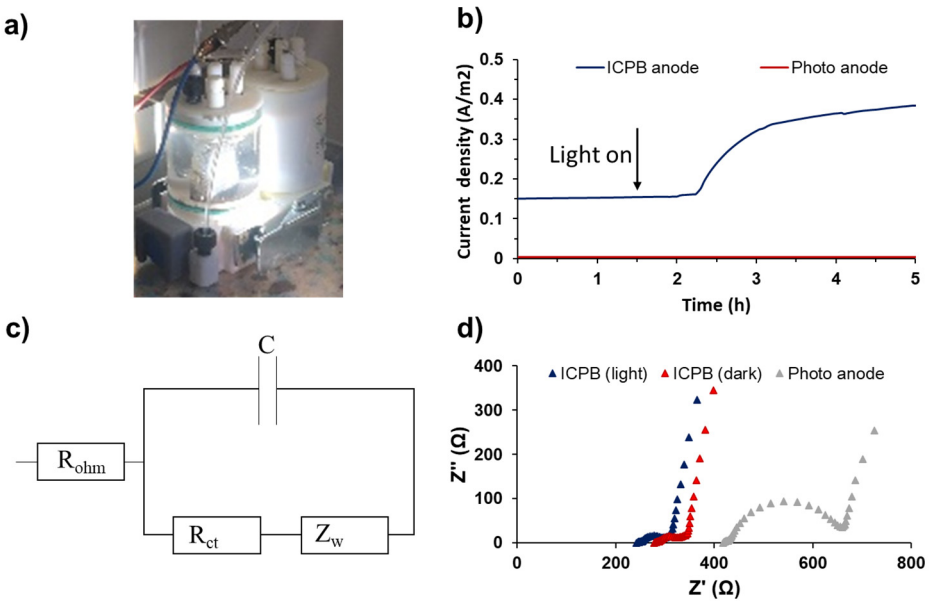

Figure 5. (**a**) s-PBEC with ICPB anode, (**b**) current densities generated by the abiotic MFC and s-PBEC with ICPB anode, (**c**) circuit equivalent used to fit anode impedance spectra, and (**d**) EIS analysis for the abiotic MFC and s-PBEC operated with ICPB anode.

The electron transfer efficiency of the ICPB anode was further investigated by EIS. According to the Nyquist plot (Figure 5c), the illuminated ICPB anode exhibited lower ohmic resistance (R_{ohm}) (240.6 Ω) compared to the ICPB (dark) (276.1 Ω), both significantly lower than the R_{ohm} of 415.3 Ω for the photoanode (without inoculation). More significantly, the lower charge-transfer resistance (R_{ct}) value of 85.6 Ω for ICPB (light) compared to ICPB (dark) (112.6 Ω) could be explained by the photogenerated electron holes that reduce the charge-transfer resistance.

To further study the electrochemical performance of EAB in ICPB anodic biofilm, LSV analysis was performed for MFCs (Figure 6). LSV is a well-known electrochemical technique where the cell potential is swept linearly in time, and the current response is plotted as a function of voltage [37]. The impact of light illumination on the ICPB anode and the response of the EAB to changes in cell voltage could be demonstrated through LSV analysis. As depicted in Figure 6, the illumination of the ICPB anode resulted in an increase in current generation from 121.0 μA to 136.9 μA. The maximum power output obtained for illuminated and dark ICPB anodes were 91.5 and 66.0 mW/m^2, respectively. The maximum current generation and power outputs obtained by the photoanode without inoculation were negligible (2.23 μA and 0.01 mW, respectively). This suggests that the enhanced current generation and power outputs achieved by the illuminated ICPB anode were due to the synergy between photocatalysis and EAB and the role of the $Co_3(PO_4)_2/Mg(OH)_2$ photocatalyst as a redox mediator to regulate EET on biofilm.

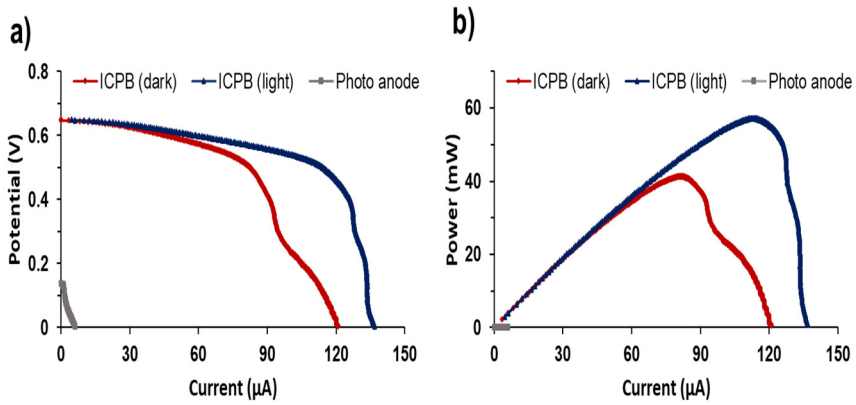

Figure 6. (**a**) Polarisation curves and (**b**) power outputs for the MFCs with ICPB anode.

3.3. Microbial Community Analysis

MESs employ microorganisms as biocatalysts for electrochemical oxidation of organic compounds. Certain microorganisms, known as EAB, have the ability to use electrodes as terminal acceptors of the electrons released during substrate oxidation. Microbial community composition and diversity in MESs are strongly affected by substrate type and its biodegradability [38]. Therefore, the composition of the anodic microbial community plays a vital role in the operation and performance of a microbial electrochemical system [37,38].

The composition of the microbial communities colonizing anodic biofilms was analysed at the level of phylum, class, and genus to identify the dominant microbial populations in ICPB anodes and investigate the effect of light exposure on changing microbial community composition (Figure 7a). The composition of the electroactive biofilm was analyzed before and after the photo-assisted experiments to evaluate the effect of light exposure and, subsequently, photo-generated electrons on the microbial community composition and the electrochemical performances. It is well-documented that photocatalysis may enhance extracellular electron transfer; therefore, it affects the interactions between bacteria in the biofilm, leading to changes in community composition [1,39].

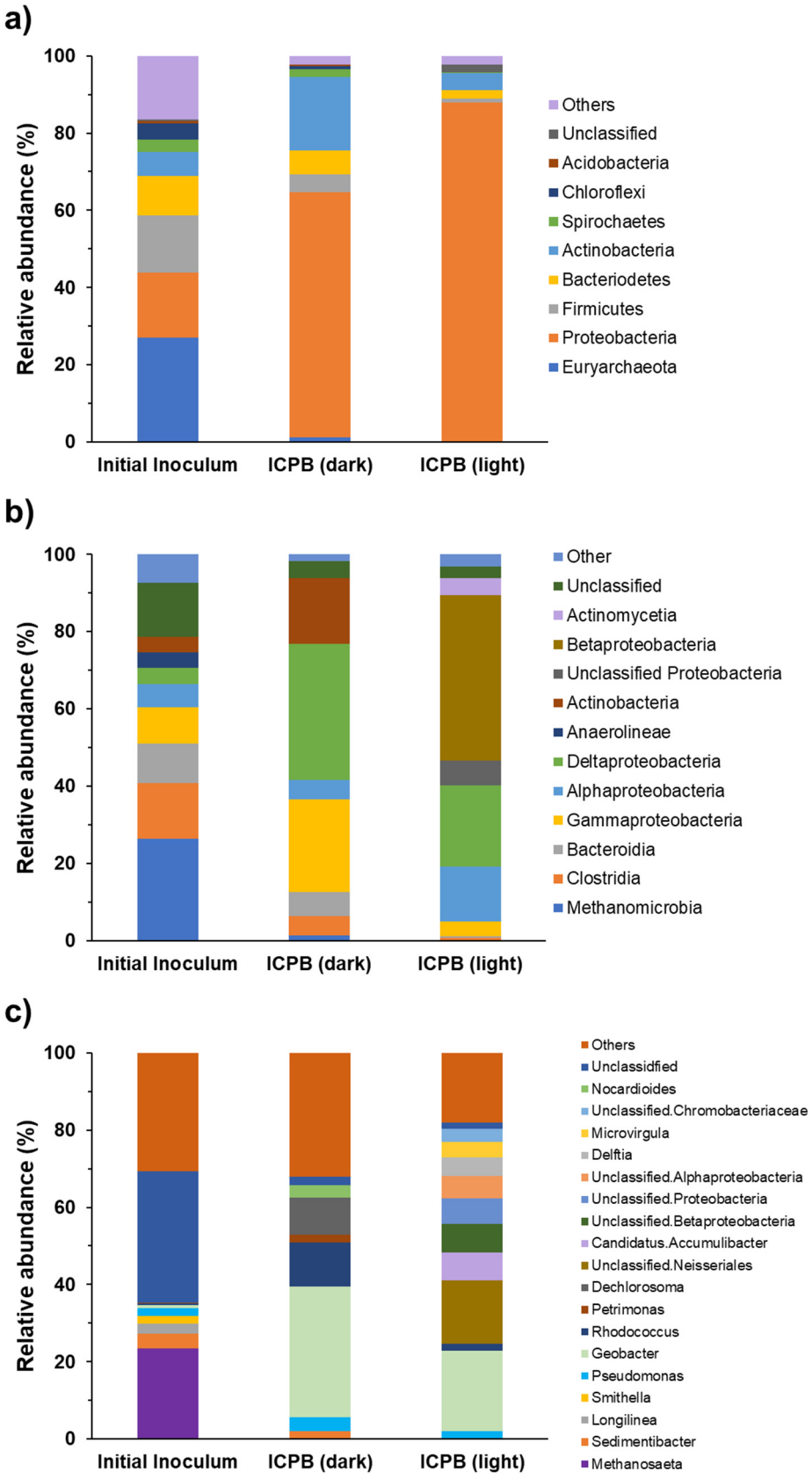

Figure 7. Composition of microbial communities on MFC anodic biofilms at (**a**) phylum, (**b**) class, and (**c**) genus levels.

The relative abundances of several phyla decreased significantly on illuminated ICPB anodes compared to ICPB in the dark. These include *Actinobacteria* (from 19.11 to 4.47%), *Bacteriodetes* (from 6.05 to 2.04%), and *Firmicutes* (from 4.79 to 1.05%). In contrast, the relative abundances of *Proteobacteria* increased from 63.40% (ICPB in the dark) to 87.93% for the illuminated ICPB). *Proteobacteria* were the main abundant phylum on ICPB anodes both in dark and light conditions. Before illumination, the most abundant classes of ICPB anodes were *delta-Proteobacteria* (35.21%), *gamma-Proteobacteria* (23.99%), and *Actinobacteria* (17.04%) (Figure 7b). Light exposure of the ICPB anode caused a significant shift in abundant classes, with *Betaproteobacteria* (42.74%), *delta-Proteobacteria* (21.12%), and *alpha-Proteobacteria* (14.16%) emerging as the most abundant classes (Figure 7b). These results are in line with the previously reported increased abundance of *Proteobacteria* in light conditions [40,41].

The changes in the microbial composition of anodic biofilms before and after illumination were more evident at the genus level (Figure 7c). Before exposure to light, the electroactive biofilm on the ICPB anode was mainly dominated by *Geobacter* (33.85%), *Rhodococcus* (11.40%), and *Dechlorosoma* (9.79%), all of which experienced decreased relative abundances after illumination (20.81%, 1.83%, and 0.01%, respectively), suggesting that they were outcompeted by other EAB. *Geobacter* are electroactive bacteria extensively found in anodic biofilms, which can donate electrons to electrodes without the requirement for natural or artificial electron shuttles [42–44]. Although the relative abundance of *Geobacter* after illumination was lower than in the dark condition, it remained the most abundant genus in the ICPB anode exposed to light. This contrasted with a study that reported a significant increase in the abundance of *Geobacter* (from 62% to 85%) using a photobioanode made of α-Fe_2O_3 photocatalyst [15]. This contradiction could result from the differences in microbial community composition and the band-edge positions of photocatalysts affecting the acceptance of photo-generated electrons by the biofilm bacteria. *Pseudomonas* was among the abundant genera on the ICPB anodes in both dark and light conditions (3.47% and 2.0%, respectively). Members of the genus *Pseudomonas* have been extensively studied for the bioremediation of contaminated environments due to their capacity for pollutant removal, allowing them to survive in a wide range of environmental conditions [45,46].

Light exposure led to the emergence of genera that were not initially among the most abundant. A diverse range of unclassified genera, mostly belonging to *Proteobacteria,* increased in abundance in the illuminated ICPB anode. These include *Unclassified. Neisseriales* (16.31%), *Unclassified. Betaproteobacteria* (7.37%), *Unclassified. Alphaproteobacteria* (5.77%), and *Unclassified. Chromobacteriaceae* (3.29%). *Candidates. Accumulibacter*, another abundant genus on illuminated ICPB anodes (7.19%), is widely found in wastewater treatment plants due to its capabilities for the simultaneous removal of phosphate and nitrate [47]. The increased abundance of *C. Accumulibacter* in activated sludge in the presence of TiO_2 and $TiCl_4$ nanoparticles has been reported previously [48,49].

Some of the less-studied genera found in illuminated ICPB anodes, including *Delftia*, *Microvirgula*, *Achromobacter*, and *Stenotrophomonas*, are known for their metabolic activities to degrade a range of pollutants from hydrocarbons to pharmaceuticals and herbicides [50–52]. The shotgun metagenomic analysis indicated that photocatalysis may indirectly result in the enrichment of light-responsive bacteria by creating selective pressure for those capable of a high rate of EET.

4. Conclusions

Our study demonstrates the capability of s-PBEC to generate an electric current from organic matter, representing an efficient approach to solving the complex waste management challenge, reducing costs related to traditional waste treatment facilities, and producing sustainable forms of energy. In this unique configuration, an abiotic photoanode able to degrade recalcitrant organic matter into readily biodegradable organic compounds is integrated with a bioanode colonized by an electroactive biofilm for electricity generation. In our study, we used a carbon foam-coated 2D/2D $Co_3(PO_4)_2/Mg(OH)_2$ heterojunction photoanode to improve electricity generation. Applying the ICPB electrode in an s-PBEC

resulted in a rapid increase in current density (0.15 A/m^2 to 0.32 A/m^2) within 1 h of light exposure, confirming the synergy between photocatalytic processes and EAB. High-throughput sequencing of the microbial community in the bioanode showed high electricity generation in s-PBEC is associated with the emergence of unclassified genera, underscoring the importance of further characterizing these microbes for enhanced s-PBEC performance. The developed hybrid electrode presents an opportunity for in-depth exploration regarding the degradation of various recalcitrant pollutants. Optimization of the dark/light cycles' duration is recommended to maximize both electricity generation and the degradation of persistent pollutants.

Author Contributions: R.R., M.M., F.E.-G. and C.A.R. conceived and designed the experiments. R.R. and M.S.A.-W. performed the experiments. R.R., A.S. and D.F. extracted and processed DNA and performed bioinformatic analysis. M.S.A.-W. and T.A.G.-A. designed and prepared the photocatalysts. R.R., M.S.A.-W., T.A.G.-A. and M.M. analyzed the data. R.R., M.S.A.-W., T.A.G.-A. and M.M. wrote the paper. F.E.-G. and C.A.R. supervised the project and were responsible for funding acquisition and revising the paper. All authors have read and agreed to the published version of the manuscript.

Funding: This work was supported by a Newton-Mosharafa Fund Institutional Link Grant from the British Council (Grant no. 352368074) and the Science, Technology, and Innovation Funding Authority (STDF), Egypt (Grant no. 30901).

Data Availability Statement: Dataset available upon request from the authors.

Conflicts of Interest: The authors declare no conflicts of interest. The funders had no role in the design of the study, in the collection, analyses, or interpretation of data, in the writing of the manuscript, or in the decision to publish the results.

Abbreviations

CB	Conduction Band
DRS	Diffuse Reflectance Spectra
EAB	Electroactive Bacteria
EET	Extracellular Electron Transfer
EIS	Electrochemical Impedance Spectroscopy
HR-TEM	High-Resolution Transmission Electron Microscope
ICPB	Intimate Coupling of Photocatalysis and Biodegradation
LSV	Linear Sweep Voltammetry
MFC	Microbial Fuel Cells
MES	Microbial Electrochemical Systems
PL	Photoluminescence
ROSs	Reactive Oxygen Species
s-PBEC	Solar-driven Photo-Bioelectrochemical Cell
TEM	Transmission Electron Microscopy

References

1. Rafieenia, R.; Sulonen, M.; Mahmoud, M.; El-Gohary, F.; Rossa, C.A. Integration of Microbial Electrochemical Systems and Photocatalysis for Sustainable Treatment of Organic Recalcitrant Wastewaters: Main Mechanisms, Recent Advances, and Present Prospects. *Sci. Total Environ.* **2022**, *824*, 153923. [CrossRef] [PubMed]
2. Wahaab, R.A.; Mahmoud, M.; van Lier, J.B. Toward Achieving Sustainable Management of Municipal Wastewater Sludge in Egypt: The Current Status and Future Prospective. *Renew. Sustain. Energy Rev.* **2020**, *127*, 109880. [CrossRef]
3. Rasheed, T.; Bilal, M.; Nabeel, F.; Adeel, M.; Iqbal, H.M.N. Environmentally-Related Contaminants of High Concern: Potential Sources and Analytical Modalities for Detection, Quantification, and Treatment. *Environ. Int.* **2019**, *122*, 52–66. [CrossRef] [PubMed]
4. Yan, Z.; Yang, X.; Lu, G.; Liu, J.; Xie, Z.; Wu, D. Potential Environmental Implications of Emerging Organic Contaminants in Taihu Lake, China: Comparison of Two Ecotoxicological Assessment Approaches. *Sci. Total Environ.* **2014**, *470–471*, 171–179. [CrossRef] [PubMed]
5. Gude, V.G. Wastewater Treatment in Microbial Fuel Cells—An Overview. *J. Clean Prod.* **2016**, *122*, 287–307. [CrossRef]

6. Vinayak, V.; Khan, M.J.; Varjani, S.; Saratale, G.D.; Saratale, R.G.; Bhatia, S.K. Microbial Fuel Cells for Remediation of Environmental Pollutants and Value Addition: Special Focus on Coupling Diatom Microbial Fuel Cells with Photocatalytic and Photoelectric Fuel Cells. *J. Biotechnol.* **2021**, *338*, 5–19. [CrossRef] [PubMed]
7. Mahmoud, M.; Parameswaran, P.; Torres, C.I.; Rittmann, B.E. Fermentation Pre-Treatment of Landfill Leachate for Enhanced Electron Recovery in a Microbial Electrolysis Cell. *Bioresour. Technol.* **2014**, *151*, 151–158. [CrossRef] [PubMed]
8. Khater, D.Z.; Amin, R.S.; Zhran, M.O.; Abd El-Aziz, Z.K.; Mahmoud, M.; Hassan, H.M.; El-Khatib, K.M. The Enhancement of Microbial Fuel Cell Performance by Anodic Bacterial Community Adaptation and Cathodic Mixed Nickel–Copper Oxides on a Graphene Electrocatalyst. *J. Genet. Eng. Biotechnol.* **2022**, *20*, 12. [CrossRef] [PubMed]
9. El-Qelish, M.; Mahmoud, M. Overcoming Organic Matter Limitation Enables High Nutrient Recovery from Sewage Sludge Reject Water in a Self-Powered Microbial Nutrient Recovery Cell. *Sci. Total Environ.* **2022**, *802*, 149851. [CrossRef] [PubMed]
10. Mahmoud, M. Electricity-Driven Microbial Factory for Value-Added Resources Recovery from Waste Streams. In *Bioelectrochemical Systems*; Volume 1 Principles and Processes; Springer: Singapore, 2020; pp. 119–138.
11. Santoro, C.; Arbizzani, C.; Erable, B.; Ieropoulos, I. Microbial Fuel Cells: From Fundamentals to Applications. A Review. *J. Power Sources* **2017**, *356*, 225–244. [CrossRef]
12. Mahmoud, M.; El-Khatib, K.M. Three-Dimensional Graphitic Mesoporous Carbon-Doped Carbon Felt Bioanodes Enables High Electric Current Production in Microbial Fuel Cells. *Int. J. Hydrog. Energy* **2020**, *45*, 32413–32422. [CrossRef]
13. Yaqoob, A.A.; Ibrahim, M.N.M.; Guerrero-Barajas, C. Modern Trend of Anodes in Microbial Fuel Cells (MFCs): An Overview. *Environ. Technol. Innov.* **2021**, *23*, 101579. [CrossRef]
14. Feng, H.; Liang, Y.; Guo, K.; Li, N.; Shen, D.; Cong, Y.; Zhou, Y.; Wang, Y.; Wang, M.; Long, Y. Hybridization of Photoanode and Bioanode to Enhance the Current Production of Bioelectrochemical Systems. *Water Res.* **2016**, *102*, 428–435. [CrossRef] [PubMed]
15. Marsolek, M.D.; Torres, C.I.; Hausner, M.; Rittmann, B.E. ARTICLE Intimate Coupling of Photocatalysis and Biodegradation in a Photocatalytic Circulating-Bed Biofilm Reactor. *Biotechnol. Bioeng* **2008**, *101*, 83–92. [CrossRef] [PubMed]
16. Zhou, D.; Dong, S.; Ki, D.; Rittmann, B.E. Photocatalytic-Induced Electron Transfer via Anode-Respiring Bacteria (ARB) at an Anode That Intimately Couples ARB and a TiO_2 Photocatalyst. *Chem. Eng. J.* **2018**, *338*, 745–751. [CrossRef]
17. Zhou, D.; Dong, S.; Shi, J.; Cui, X.; Ki, D.; Torres, C.I.; Rittmann, B.E. Intimate Coupling of an N-Doped TiO_2 Photocatalyst and Anode Respiring Bacteria for Enhancing 4-Chlorophenol Degradation and Current Generation. *Chem. Eng. J.* **2017**, *317*, 882–889. [CrossRef]
18. Zhu, Q.; Wang, X.; Hu, J.; Chen, S.; Hu, S.; Wu, Y.; Liu, B.; Xiao, K.; Liang, S.; Yang, J.; et al. Efficient Degradation of Refractory Pollutant in a Microbial Fuel Cell with Novel Hybrid Photocatalytic Air-Cathode: Intimate Coupling of Microbial and Photocatalytic Processes. *Bioresour. Technol.* **2021**, *340*, 125717. [CrossRef] [PubMed]
19. Wang, X.; Hu, J.; Chen, Q.; Zhang, P.; Wu, L.; Li, J.; Liu, B.; Xiao, K.; Liang, S.; Huang, L. Synergic Degradation of 2, 4, 6-Trichlorophenol in Microbial Fuel Cells with Intimately Coupled Photocatalytic-Electrogenic Anode. *Water Res.* **2019**, *156*, 125–135. [CrossRef] [PubMed]
20. Wang, C.; Wu, G.; Zhu, X.; Xing, Y.; Yuan, X.; Qu, J. Synergistic Degradation for O-Chlorophenol and Enhancement of Power Generation by a Coupled Photocatalytic-Microbial Fuel Cell System. *Chemosphere* **2022**, *293*, 133517. [CrossRef]
21. Antolini, E. Photoelectrocatalytic Fuel Cells and Photoelectrode Microbial Fuel Cells for Wastewater Treatment and Power Generation. *J. Environ. Chem. Eng.* **2019**, *7*, 103241. [CrossRef]
22. Yu, M.; Wang, J.; Tang, L.; Feng, C.; Liu, H.; Zhang, H.; Peng, B.; Chen, Z.; Xie, Q. Intimate Coupling of Photocatalysis and Biodegradation for Wastewater Treatment: Mechanisms, Recent Advances and Environmental Applications. *Water Res.* **2020**, *175*, 115673. [CrossRef]
23. Wang, H.; Liu, X.; Niu, P.; Wang, S.; Shi, J.; Li, L. Porous Two-Dimensional Materials for Photocatalytic and Electrocatalytic Applications. *Matter* **2020**, *2*, 1377–1413. [CrossRef]
24. Gan, X.; Lei, D.; Wong, K.-Y. Two-Dimensional Layered Nanomaterials for Visible-Light-Driven Photocatalytic Water Splitting. *Mater. Today Energy* **2018**, *10*, 352–367. [CrossRef]
25. Zhu, M.; Han, M.; Zhu, C.; Hu, L.; Huang, H.; Liu, Y.; Kang, Z. Strong Coupling Effect at the Interface of Cobalt Phosphate-Carbon Dots Boost Photocatalytic Water Splitting. *J. Colloid Interface Sci.* **2018**, *530*, 256–263. [CrossRef]
26. Wang, B.-J.; Li, X.-H.; Cai, X.-L.; Yu, W.-Y.; Zhang, L.-W.; Zhao, R.-Q.; Ke, S.-H. Blue Phosphorus/$Mg(OH)_2$ van Der Waals Heterostructures as Promising Visible-Light Photocatalysts for Water Splitting. *J. Phys. Chem. C* **2018**, *122*, 7075–7080. [CrossRef]
27. Mahmoud, M.; Torres, C.I.; Rittmann, B.E. Changes in Glucose Fermentation Pathways as a Response to the Free Ammonia Concentration in Microbial Electrolysis Cells. *Environ. Sci. Technol.* **2017**, *51*, 13461–13470. [CrossRef]
28. Tamames, J.; Puente-Sánchez, F. SqueezeMeta, A Highly Portable, Fully Automatic Metagenomic Analysis Pipeline. *Front. Microbiol.* **2019**, *9*, 425882. [CrossRef]
29. Li, D.; Liu, C.-M.; Luo, R.; Sadakane, K.; Lam, T.-W. MEGAHIT: An Ultra-Fast Single-Node Solution for Large and Complex Metagenomics Assembly via Succinct de Bruijn Graph. *Bioinformatics* **2015**, *31*, 1674–1676. [CrossRef]
30. Wu, Y.-W.; Simmons, B.A.; Singer, S.W. MaxBin 2.0: An Automated Binning Algorithm to Recover Genomes from Multiple Metagenomic Datasets. *Bioinformatics* **2016**, *32*, 605–607. [CrossRef] [PubMed]
31. Kang, D.D.; Li, F.; Kirton, E.; Thomas, A.; Egan, R.; An, H.; Wang, Z. MetaBAT 2: An Adaptive Binning Algorithm for Robust and Efficient Genome Reconstruction from Metagenome Assemblies. *PeerJ* **2019**, *7*, e7359. [CrossRef] [PubMed]

32. Shao, H.; Padmanathan, N.; McNulty, D.; O'Dwyer, C.; Razeeb, K.M. Supercapattery Based on Binder-Free $Co_3(PO_4)_2 \cdot 8H_2O$ Multilayer Nano/Microflakes on Nickel Foam. *ACS Appl. Mater. Interfaces* **2016**, *8*, 28592–28598. [CrossRef]
33. Li, J.; Zhang, L.; Yang, P.; Cheng, X. Morphological Evolution of Co Phosphate and Its Electrochemical and Photocatalytic Performance. *CrystEngComm* **2018**, *20*, 6982–6988. [CrossRef]
34. Kang, J.; Keikhaei, M.; Li, T.; Ichimura, M. Galvanostatic Electrochemical Deposition of Cu-Doped $Mg(OH)_2$ Thin Films and Fabrication of Pn Homojunction. *Mater. Res. Bull.* **2021**, *137*, 111207. [CrossRef]
35. Aggoun, K.; Chaal, L.; Creus, J.; Sabot, R.; Saidani, B.; Jeannin, M. Marine Corrosion Resistance of $CeO_2/Mg(OH)_2$ Mixed Coating on a Low Alloyed Steel. *Surf. Coat. Technol.* **2019**, *372*, 410–421. [CrossRef]
36. Suslu, A.; Wu, K.; Sahin, H.; Chen, B.; Yang, S.; Cai, H.; Aoki, T.; Horzum, S.; Kang, J.; Peeters, F.M. Unusual Dimensionality Effects and Surface Charge Density in 2D Mg $(OH)_2$. *Sci. Rep.* **2016**, *6*, 20525. [CrossRef]
37. Saratale, R.G.; Saratale, G.D.; Pugazhendhi, A.; Zhen, G.; Kumar, G.; Kadier, A.; Sivagurunathan, P. Microbiome Involved in Microbial Electrochemical Systems (MESs): A Review. *Chemosphere* **2017**, *177*, 176–188. [CrossRef]
38. Logan, B.E.; Regan, J.M. Electricity-Producing Bacterial Communities in Microbial Fuel Cells. *Trends Microbiol.* **2006**, *14*, 512–518. [CrossRef]
39. Ahtesham, A.; Shahadat, M.; Hussain, E.; Adnan, R.; Ahammad, S.Z.; Jain, R.; Raees, K. Treatment of Antibiotic-Resistant Genes via Photocatalytic-Assisted Microbial Fuel Cells: A Review. *J. Water Process Eng.* **2023**, *55*, 104126. [CrossRef]
40. Guan, J.; Cao, X.; Yuan, Y.; Wang, C.; An, R.; Lu, P.; Lu, N. Synergic Mechanisms of Electricity Generation and Bisphenol a Degradation in a Novel Photocatalytic-Microbial Fuel Cell Equipped with a TiO_2-C-$BiVO_4$ Photo-Anode and a Biofilm-Anode. *Chem. Eng. J.* **2023**, *471*, 144308. [CrossRef]
41. Xu, Y.; Zhang, N.; Yang, G.; Chang, Y.; Wang, D.; Xia, J. Degradation Mechanisms and Microbial Community Analysis of Cefalexin in the Intimately Coupled Photocatalytic and Biodegradation System. *Energy Rep.* **2023**, *9*, 206–218. [CrossRef]
42. Long, X.; Wang, H.; Wang, C.; Li, X. The Synergistic Effect of Biophoto Anode for the Enhancement of Current Generation and Degradation. *Environ. Technol.* **2020**, *41*, 3420–3430. [CrossRef]
43. Hou, Y.; Yuan, G.; Qin, S.; Tu, L.; Yan, Y.; Yu, Z.; Lin, H.; Chen, Y.; Zhu, H.; Song, H.; et al. Photocathode Optimization and Microbial Community in the Solar-Illuminated Bio-Photoelectrochemical System for Nitrofurazone Degradation. *Bioresour. Technol.* **2020**, *302*, 122761. [CrossRef]
44. Rafieenia, R.; Mahmoud, M.; El-Gohary, F.; Avignone Rossa, C. The Degradation of Glyphosate Is Enhanced in a Microbial Fuel Cell: Electrochemical Performance, Degradation Efficiency, and Analysis of the Anodic Microbial Community. *Sustain. Energy Technol. Assess.* **2022**, *54*, 102805. [CrossRef]
45. Yang, Y.; Pratap Singh, R.; Song, D.; Chen, Q.; Zheng, X.; Zhang, C.; Zhang, M.; Li, Y. Synergistic Effect of Pseudomonas Putida II-2 and Achromobacter Sp. QC36 for the Effective Biodegradation of the Herbicide Quinclorac. *Ecotoxicol. Environ. Saf.* **2020**, *188*, 109826. [CrossRef]
46. Safdari, M.-S.; Kariminia, H.-R.; Ghobadi Nejad, Z.; Fletcher, T.H. Study Potential of Indigenous Pseudomonas Aeruginosa and Bacillus Subtilis in Bioremediation of Diesel-Contaminated Water. *Water Air Soil Pollut.* **2017**, *228*, 1–7. [CrossRef]
47. Petriglieri, F.; Singleton, C.M.; Kondrotaite, Z.; Dueholm, M.K.D.; McDaniel, E.A.; McMahon, K.D.; Nielsen, P.H. Reevaluation of the Phylogenetic Diversity and Global Distribution of the Genus "*Candidatus* Accumulibacter". *mSystems* **2022**, *7*, e00016–e00022. [CrossRef]
48. Li, Z.; Wang, X.; Ma, B.; Wang, S.; Zheng, D.; She, Z.; Guo, L.; Zhao, Y.; Xu, Q.; Jin, C.; et al. Long-Term Impacts of Titanium Dioxide Nanoparticles (TiO_2 NPs) on Performance and Microbial Community of Activated Sludge. *Bioresour. Technol.* **2017**, *238*, 361–368. [CrossRef]
49. Jia, Y.; Zeng, W.; Fan, Z.; Meng, Q.; Liu, H.; Peng, Y. An Effective Titanium Salt Dosing Strategy for Phosphorus Removal from Wastewater: Synergistic Enhancement of Chemical and Biological Treatment. *Sci. Total Environ.* **2022**, *842*, 156960. [CrossRef]
50. Leibeling, S.; Schmidt, F.; Jehmlich, N.; von Bergen, M.; Müller, R.H.; Harms, H. Declining Capacity of Starving *Delftia Acidovorans* MC1 to Degrade Phenoxypropionate Herbicides Correlates with Oxidative Modification of the Initial Enzyme. *Environ. Sci. Technol.* **2010**, *44*, 3793–3799. [CrossRef]
51. Subhash, Y.; Park, M.-J.; Lee, S.-S. Microvirgula Curvata Sp. Nov., Isolated from Hydrocarbon-Contaminated Soil, and Emended Description of the Genus Microvirgula. *Int. J. Syst. Evol. Microbiol.* **2016**, *66*, 5309–5313. [CrossRef] [PubMed]
52. Sauvetre, A.; Schroder, P. Uptake of Carbamazepine by Rhizomes and Endophytic Bacteria of Phragmites Australis. *Front. Plant Sci.* **2015**, *6*, 128336. [CrossRef]

Disclaimer/Publisher's Note: The statements, opinions and data contained in all publications are solely those of the individual author(s) and contributor(s) and not of MDPI and/or the editor(s). MDPI and/or the editor(s) disclaim responsibility for any injury to people or property resulting from any ideas, methods, instructions or products referred to in the content.